J Mater Sci: Mater Med (2010) 21:2009–2020
DOI 10.1007/s10856-010-4064-y

Surfactant-modified β-TCP: structure, properties, and in vitro remineralization of subsurface enamel lesions

Robert L. Karlinsey · Allen C. Mackey · Emily R. Walker · Katherine E. Frederick

Received: 13 May 2009 / Accepted: 20 March 2010 / Published online: 3 April 2010

Abstract A hybrid material comprised of beta-tricalcium phosphate (β-TCP) and sodium lauryl sulfate (SLS) was prepared using a mechanochemical process, examined using particle size analysis, IR spectroscopy, ^{31}P, ^{23}Na, and ^{13}C solid-state NMR spectroscopy, and calcium dissolution experiments, and probed for in vitro remineralization of subsurface enamel lesions. Our results suggest that while the ^{31}P environments of β-TCP remain unchanged during solid-state processing, there is noticeable shifting among the SLS ^{23}Na and ^{13}C environments. Therefore, given the structure of β-TCP, along with our IR examinations and calcium dissolution isotherms, SLS appears to interface strongly with the cation deficient C_3 symmetry site of the β-TCP hexagonal crystal lattice with probable emphasis placed on the underbonded CaO_3 polyhedra. To demonstrate the utility of the surface-active TCP material in dental applications, we combined the TCP–SLS with 5,000 ppm F (NaF) and evaluated the remineralization potential of subsurface enamel lesions via an in vitro remineralization/demineralization pH cycling dental model. Using surface and longitudinal microhardness measurements, the TCP–SLS plus 5,000 ppm F system was found to significantly boost remineralization of subsurface enamel lesions, with microhardness values increasing up to 30% greater than fluoride alone.

R. L. Karlinsey (✉) · A. C. Mackey · E. R. Walker · K. E. Frederick
Indiana Nanotech, 351 W. 10th Street, Suite 309, Indianapolis, IN 46202, USA
e-mail: rkarlins@gmail.com

1 Introduction

Due to the relatively low levels of calcium naturally generated in the oral cavity, the need to replenish weakened teeth with the body's natural oral mineral reserves is often unmet [1]. Other means, such as fluoride, could be required to help repair the dentition. Fluoride has a rich and clinically-proven history of preventing dental decay [2–5]. First added to drinking water in low levels [6, 7], topical fluorides have evolved into such common vehicles as toothpaste and mouthrinses [8]. These relatively inexpensive forms of dental therapy are quite appealing and will likely become even more so as the views of patients and practitioners shift even further to prevention instead of restoration, the latter of which is typically considered to be more costly and painful.

Unfortunately, even with fluoride and other preventive measures, dental decay still affects the majority of the world's population [9], with its etiology arising from genetic disorders, eating habits and diet choices, behavioral habits, and naturally occurring physicochemical processes in the mouth [10]. In fact a US study by the National Health and Nutrition Examination Survey recently reported that while dental decay has not increased in the last 25 years for most of the US population, dental decay is on the rise in children between 2 and 11 years old [11]. This apparent epidemic suggests that fluoride alone, despite its great clinical success and acceptance, may be insufficient.

From a chemical treatment perspective, promising attempts in improving dental remineralization have included interfacing fluoride with other minerals, such as calcium, phosphate, strontium, etc., with calcium considered as the essential component to the repair of weakened teeth [12–14]. Separately, innovative calcium phosphate materials that work in the absence of fluoride, such as bioactive glass,

amorphous calcium phosphate, and milk-derived protein complexes containing calcium, have been developed [15, 16]. Though promising, such innovative calcium phosphates can compromise bioavailable fluoride, and therefore, therapeutic efficacy [4]. This is largely due to the reactivity of bioavailable fluoride and calcium, which rapidly form calcium fluoride [17] when introduced together in an aqueous rinse or dentifrice prior to reaching the dentition during an oral hygienic event [18]. Therefore, the ability to devise a calcium material that can coexist with fluoride to provide greater efficacy relative to fluoride alone presents an opportunity to further the therapeutic effects of fluoride to provide enhanced dental health benefits.

Recently we reported on preliminary studies demonstrating the synthesis and fluoride compatibility of an innovative calcium phosphate system comprised of surfactant-modified beta-tricalcium phosphate (β-TCP) [19]. In this paper we describe in detail the structure, properties, and hard-tissue response of β-TCP that has been modified with an ionic surfactant (sodium lauryl sulfate, SLS) using a mechanochemical ball milling process. β-TCP is an appealing calcium phosphate system because it is a precursor to hydroxyapatite formation [20], is biocompatible and bioactive [21, 22], and manifests lattice defects that allow for crystal modification (e.g., the underbonded CaO_3 polyhedra lying in the C_3 symmetry site in Fig. 1) [23]. SLS is attractive due to its surface-active properties and widespread use in dental formulations [24, 25]. Using a mechanochemical process, we hypothesize that a modified β-TCP material can be constructed by exploiting the defects in the TCP lattice with SLS. To demonstrate the therapeutic promise of the TCP–SLS material when

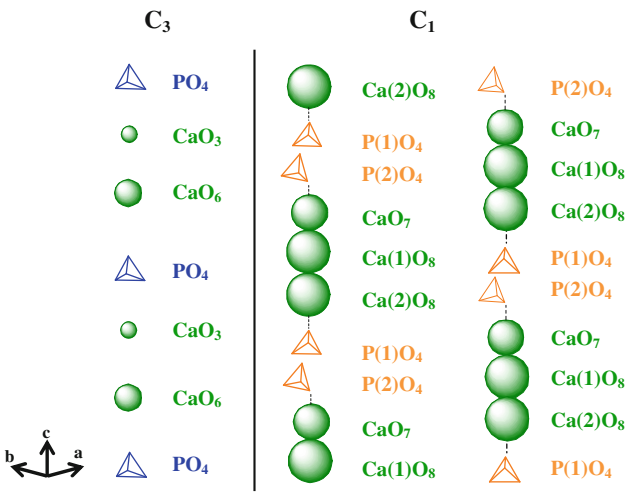

Fig. 1 Schematic of the tow symmetry sites, C_3 and C_1, of the β-TCP unit cell. Adaptation of the unit cell structure is based on neutron diffraction data published by Yashima et al. [34]. Identifications of the calcium and phosphate polyhedra are shown immediately to the right

combined with fluoride, we evaluated the efficacy of TCP–SLS plus 5,000 ppm F (NaF) relative to 5,000 ppm F alone in remineralizing weakened enamel emulating early caries formation. The efficacy study employed herein subjects non-cavitated enamel specimens to remineralization and demineralization events and is based on widely-accepted in vitro dental models that successfully emulate the clinical situation [4, 26–30].

2 Materials and methods

2.1 TCP–SLS preparation

The TCP–SLS 'functionalized' hybrid material was created using a high impact grinding procedure described as follows. 98 wt% β-tricalcium phosphate (EP-grade, Budenheim) and 2 wt% sodium lauryl sulfate (NF-grade, Spectrum Chemical) were loaded into a 500 ml stainless steel grinding jar lined with yttrium-stabilized zirconium oxide. Also added to the jar were ten 20-mm diameter yttrium-stabilized zirconium oxide balls and 200 ml of pentane (>99%, Sigma-Aldrich), which served as a lubricant during grinding. A lid lined with zirconium oxide was then clamped tightly to the grinding jar and the grinding jar assembly was placed into a rotatable station mounted on the turntable of a PM400 planetary ball mill (Retsch), where it was secured with a quick-action locking spider clamp. Two identical sets of jars were secured in the PM400 to ensure necessary counter-balancing. The turntable speed was set to 375 rpm (jar speed was 750 rpm in the direction opposite the turntable rotation) and the grinding process lasted for a period of 2 h, with less than 5 rpm in speed variation as monitored with a CDT-100 hand-held tachometer (Check-Line). After the grinding process was completed, the jar system was carefully opened in a fume hood with the resultant slurry deposited into a collection pan fitted with a sieve. The pan was then placed into a vacuum oven at ~45°C (Fisher Scientific) and gently evacuated to a pressure of −29 in Hg (Ashcroft) at which point the pressure inside the vacuum oven did not increase when the oven valve to the vacuum pump was closed for at least 30 s. The off-white dried powder was then funneled into graduated HDPE plastic bottles and stored until use. The loss on drying was near 0.0% (USP method <731>) and the true density (Micromeritics AccuPyc 1330 Helium Pycnometer) was 2.97 g/cc (USP method <699>).

2.2 Particle size

Particle size measurements were performed using a Malvern Mastersizer 2000 LASER diffractor fitted with a

Hydro 2000S sampler. The sampler was filled with 20 ml of 0.2 μm filtered distilled water and 1–2 ml of 4% sodium pyrophosphate (Fisher Scientific) added to help facilitate dispersion. Aliquots of the TCP–SLS material were then added and sonicated for 10 min to create the suspension. Four individual runs with a 60-s delay between each run were performed on each sample suspension and averaged to generate the particle size distribution. To ensure accurate data collection, particle size distributions were collected on standards comprising borosilicate glass microspheres (Duke Scientific) immersed in a distilled water solution containing a non-ionic surfactant and were found to be within ±3% of the NIST-certified size range. The Malvern software calculates the particle distributions based on equivalent spherical diameters, which generates a differential histogram, as well as d(10%), d(50%), and d(90%) values, for both TCP–SLS and β-TCP.

2.3 IR spectroscopy

Infrared spectroscopy on KBr-based pellets was performed using an M500 dispersive IR spectrometer (Buck Scientific) at a resolution of 2 cm^{-1} with spectra collected between 2,000 and 600 cm^{-1}. Polystyrene film was used as a reference material. Prior to collecting data, KBr powder was dried under vacuum (−28 in Hg) in a vacuum oven at 105°C for 3 h. Using an analytical balance (OHAUS), sample masses of 1 mg were combined with 100 mg KBr and vigorously dispersed using an agate mortar and pestle, resulting in a white sample–matrix mixture having the texture of fine flour. Approximately 55 mg of the mixture was placed into a beta press fitted with a steel bolt (rotated five full turns). To form an intact pellet window, the press was then placed into a vice, and using a calibrated torque wrench (Kobalt) set to 40 ft-lb, a second bolt was tightened at the other end of the press and remained undisturbed for 10 min. Afterwards, the bolts were removed and the press was inserted into the cell chamber for data acquisition. Collected data were exported from the EZ-Scan software as ASCII files and analyzed using Microcal Origin.

2.4 NMR spectroscopy

^{31}P, ^{23}Na, and ^{13}C solid-state NMR experiments were performed using a Varian UnityPlus-200 spectrometer and a dual channel Doty Scientific 7 mm Supersonic Magic Angle Spinning probe. For all studies, gated decoupling and magic angle spinning speeds of 5.5 kHz were used and 2,048 points were acquired in the FID. ^{31}P NMR parameters and experiments were performed as follows. VNMR (Varian) and MestRe-C v2.3 (Mestrelab Research) software were used to analyze NMR data. The spectrometer frequency was tuned to 80.963 MHz and the spectral width was 50 kHz. A 30° single pulse excitation 2 μs long with a 20 s relaxation delay was used to generate the FID. For T_1 inversion recovery experiments, the relaxation delay was 20 s and the delay between 180° and 90° pulses ranged between 0.06 and 128 s. Potassium phosphate was used as the reference.

^{23}Na NMR parameters and experiments were performed as follows. The spectrometer frequency was tuned to 52.907 MHz and the spectral width was 50 kHz. A 45° single pulse excitation 3 μs long with a 300 ms relaxation delay was used to generate the FID. For T_1 inversion recovery experiments, the relaxation delay was 300 ms and the delay between 180° and 90° pulses ranged between 12 μs and 410 ms. NaCl was used as the reference.

^{13}C NMR parameters and experiments were performed as follows. The spectrometer frequency was tuned to 50.297 MHz and the spectral width was 40 kHz. A 90° ^{1}H contact pulse 5.6 μs long was used for the ^{1}H–^{13}C cross-polarization (CP) studies. The relaxation delay was 8 s and the contact time was 4 ms was used to generate the FID. For CP T_1 inversion recovery experiments, the relaxation delay was 8 s and the delay between 180° and 90° pulses ranged between 100 ms and 25 s. Hexamethylbenzene was used as the reference.

2.5 Calcium availability and pH

Ionic (available) calcium was measured in triplicate using an UltraBASIC UB-10 pH/mV meter (Denver Instrument) coupled with an Orion 97-20 Ionplus calcium-sensitive electrode (Thermo Electron). A 4 M KCl solution was used as the ionic strength adjuster (ISA). The measured mV readings were converted to ppm using calibration curves. For low-content calcium (between 0.01 and 0.47 ppm Ca), standards were made with a water:ISA ratio of 100:1. For curves between 1 and 100 ppm Ca, standards with 50:1 ratios of water:ISA were prepared. Readings were recorded after addition of sample to 40 ml of water at 5 s for the first 30 s, 15 s up to 300 s (5 min), and then every minute up to 900 s (15 min). At the end of the dissolution experiment, the pH was measured using an Accumet AR10 pH meter (Fisher Scientific) calibrated to a pH = 5.0 standard solution (0.05 M potassium biphthalate sodium hydroxide buffer, Fisher Scientific). All data were analyzed using Microcal Origin software.

2.6 In vitro performance testing

Three test groups were prepared to evaluate the efficacy of fluoride versus fluoride plus the TCP–SLS material in remineralizing enamel lesions emulating early-stage caries formation: (1) distilled water (negative control); (2) 5,000 ppm F solution (NaF in distilled water, positive control); (3)

5,000 ppm F solution (NaF in distilled water) + 800 ppm TCP–SLS.

Preparation and execution of in vitro performance testing on bovine enamel were performed as follows. 3 mm enamel cores were drilled from clean bovine molars [31] and mounted in acrylic rods. The cores were then ground with 600 grit sandpaper for 2 min and polished with 0.05 μm gamma alumina for 45 min. After sonication and rinsing with distilled (DI) water, specimens were immersed in vials containing carbopol–lactic acid solution partially saturated with hydroxyapatite (BioRad) and adjusted to a pH of 5.0 [26, 32]. These vials were subsequently loaded into an incubator at 37°C to establish 'white-spot' (non-cavitated) lesions, the characteristics and histology of which have been discussed in detail previously by White [32]. Briefly, the caries-like lesions produced by this solution have a dense surface mineral zone approximately 15 μm thick (via polarized light microscopy) [32], while lesion depth extends to about 70 μm (via microradiographic analysis [32] and reflective microscopy). After immersion for 36 h, specimens were removed from the solution, rinsed with DI water, and measured for baseline Vickers microhardness (200 gf, 15 s dwell time) using a microhardness indenter (Leco, model 247AT) interfaced with Confident software (Leco). Specimens exhibiting mean Vickers hardness numbers (VHN) between 25 and 45 were selected for the study and stratified into the eight groups ($N = 9$) having an overall mean VHN of about 33 VHN (note: for reference, sound bovine enamel has typical VHN between 300 and 350).

The in vitro pH cycling model [33] included two 2-min treatment periods performed an hour apart in the morning, followed by one 4-h carbopol–lactic acid challenge, and finally two additional 2-min treatment periods in the afternoon, administered daily for a total of 5 days. Each treatment was comprised of 5 ml test solution and 10 ml distilled water. Between the daily treatments and acid challenge, specimens were immersed in artificial saliva [27]. The treatment and saliva systems were magnetically agitated at 300 rpm, while the acid challenge was static. After each treatment and acid challenge, the specimens were rinsed with DI water prior to placement into artificial saliva. Four fresh treatment slurries and fresh carbopol–lactic acid solution were used daily, with the artificial saliva solution changed once daily after the third treatment.

After the 5 days of cycling, the enamel specimens were examined for surface and longitudinal microhardness. For surface microhardness studies, the change in Vickers hardness number (ΔVHN) was determined as the difference between the post and baseline values ($\Delta VHN = VHN_{post} - VHN_{base}$), with the post value determined using the same Vickers indenter conditions (200 gf, 15 s dwell time). After surface measurements were made, longitudinal studies assessing bulk remineralization were performed as follows. A Lapcraft Lil' Trimmer circular saw was used to section the enamel specimens. The cross-sections were then mounted with ClaroCit methylmethacrylate-based cold mounting resin (Struers) with the freshly cut surfaces exposed. The mounted specimens were serially ground with 180, 600, 1,000, and 1,500 grit sandpaper (3 M), and then serially polished with 9, 3, and 1 μm polycrystalline diamond suspension (Buehler). Longitudinal microhardness was performed with the Knoops indenter fitted on the microhardness tester. A series of three indentations per specimen were made under (1) a 10 gf load at 12.5 μm, (2) a 25 gf load at 25, 37.5, and 50 μm, and (3) a 50 gf load used at 75, 100, 125, and 150 μm below the specimen surface, resulting in a total of 27 indents per specimen. The Knoops indentation lengths were then converted to Knoops Hardness Numbers (KHN).

Statistical evaluation of the microhardness data was performed using Sigma Stat software version 3.1. One-way analysis of variance (ANOVA) was used to test for significance, followed by the Student–Newman–Keuls (SNK) method to identify differences among groups ($P < 0.05$). Discordant values were excluded using the Q-test.

3 Results and discussion

3.1 TCP–SLS structure and properties

Figure 1 summarizes the nature of the calcium and phosphate polyhedra comprising the β-TCP lattice. The green spheres represent CaO_n clusters, with $n = 3$, 6, 7, or 8. The blue orthophosphate polyhedra represent unattached or 'free' phosphate, while the orange orthophosphate polyhedra represent connected or 'bound' phosphate. Within the C_3 symmetry site, the volumes of the seven polyhedra, determined by Yashima et al. [34] are as follows: PO_4: 1.87 Å^3; CaO_3: 0.67 Å^3; CaO_6: 14.71 Å^3. The polyhedra positioned in this site do not share corners or edges with neighboring polyhedra. The occupied volume of the seven polyhedra lying in the C_3 site is approximately 35.5 Å^3.

The C_1 site manifests two crystalline arrangements and the polyhedra volumes are as follows [34]: $Ca(2)O_8$: 26.08 Å^3; $P(1)O_4$: 1.86 Å^3; $P(2)O_4$: 1.85 Å^3; CaO_7: 20.46 Å^3; $Ca(1)O_8$: 25.99 Å^3. All of the polyhedra positioned in this site share either corners or edges with neighboring polyhedra. The polyhedra sharing one oxygen atom include the following pairs: $Ca(2)O_8$–$P(1)O_4$ and $P(2)O_4$–CaO_7. The polyhedra sharing two oxygen atoms include the following pairs: CaO_7–$Ca(1)O_8$ and CaO_7–$Ca(2)O_8$. The occupied volume of the 10 polyhedra in each of the two C_1 sites is approximately 152 Å^3.

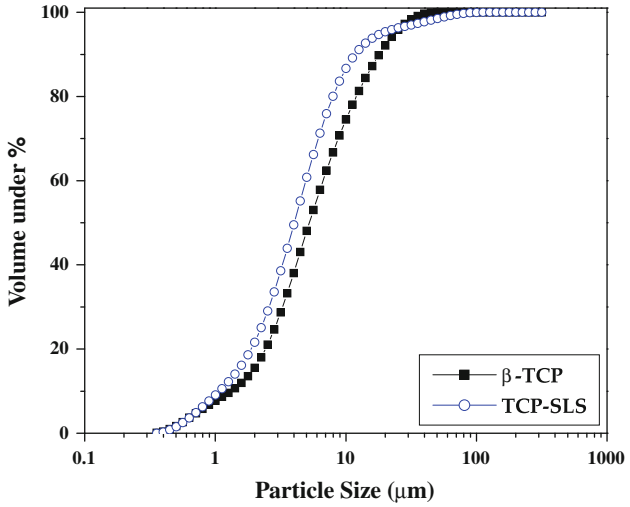

Fig. 2 Particle size distributions for β-TCP and the hybrid TCP–SLS material. Significant differences are observed for volume under % between 10 and 90%

Between the two symmetry sites, the dramatic differences in both the coordination and occupied volumes of the polyhedra suggest modifications will likely occur within the C_3 symmetry site. Further, these differences may bear on the functionalization of β-TCP with SLS as discussed below.

The particle distribution for β-TCP and the TCP–SLS functionalized material is shown in Fig. 2. The particle sizes at d(10%) for β-TCP and TCP–SLS were 1.32 and 1.00 μm, respectively. The particle size calculations at d(50%) for β-TCP and TCP–SLS were 5.25 and 3.99 μm, respectively, and the calculations at d(90%) for β-TCP and TCP–SLS were 17.98 and 15.53 μm, respectively. The standard deviations at d(10%), d(50%), and d(90%) were 0.09, 0.22, and 1.01 μm, respectively, as determined through method validation. Below d(10%) and above d(90%) the differences between the two materials are insignificant. But statistically significant differences were observed at d(10%), d(50%) and d(90%), with TCP–SLS having statistically smaller particle sizes relative to β-TCP. Thus, it appears forcibly combining β-TCP and SLS together does not create larger particles but instead produces slightly smaller particles relative to native β-TCP. This suggests the resulting impaction between β-TCP and SLS is significant enough to reduce particle size despite the simultaneous creation of a hybrid solid material manifesting properties of both reagents. Second, the particle distribution of the blended material falls within acceptable ranges of abrasion agents commonly incorporated into dentifrices, and this is important for compliance with International Standard Organization (ISO) or American Dental Association (ADA) standards for dental abrasion, for example. For instance, mean particle sizes for abrasion agents found in dentifrices often range between 1 and 20 μm. Figure 2 clearly shows the particle size at d(0.5) is similar to the mean particle size of 9 μm obtained for the dental silica Sident® 9 (Evonik-Degussa). Recently, we reported on the relative dentin and enamel abrasions of a prototype dentifrice containing the TCP–SLS material, which were found to be well within the ISO and ADA acceptability range [35].

Figure 3 reveals active IR modes of phosphate bands between 1,600 and 600 cm^{-1}. The β-TCP signature shown here agrees very well with the published work by Jillavenkatesa and Condrate [36]. The low energy mode centered around 727 cm^{-1} may correspond to the $(P–O–P)_s$ vibration characteristic of pyrophosphate, $P_2O_7^{4-}$, which can be described as manifested by one bridging oxygen [37]. Pyrophosphate, along with other calcium phosphate phases, may appear as a by-product during wet-chemical synthesis of calcium phosphates [38]. This may be the case presently since β-TCP used here is precipitated by reacting phosphoric acid and calcium hydroxide in aqueous solution and then calcined [39]. At this mode, the peak intensities between β-TCP and TCP–SLS are essentially the same and since the same KBr-TCP loading conditions were used, this suggests the SLS does not appear to significantly influence pyrophosphate during the grinding process. The remaining modes belong primarily to orthophosphate and can readily be identified with knowledge of the β-TCP structure. We have used the published results of Jillavenkatesa and Condrate [36] and Yashima et al. [34] to support our structural assignments and assessments. The vibrations near 948 and 971 cm^{-1} correspond to two symmetric P–O stretching vibrations of the fundamental v_1 mode of the 'bound' orthophosphate as shown in the C_1 symmetry site in Fig. 1. The prominent peaks spanning the spectral range between 1,020 and 1,045 cm^{-1} may be assigned to bending P–O vibrations of the v_3 IR active fundamental modes of orthophosphate environments particular to both the C_3 and C_1 symmetry sites, along with the weak higher-energy shoulders ranging between 1,071 and 1,088 cm^{-1}. Pertaining to both C_3 and C_1 phosphate environments, the strong peak centered about 1,120 cm^{-1} can be assigned to non-bridging PO ionic ($P–O^-$) vibrational stretching, while the P=O stretch occurs near 1,215 cm^{-1} [37].

Judging by similarities in the bandshape widths across the spectral range shown in Fig. 3, significant modification in long-range order due to milling may not be the primary factor leading to diminished peak intensities; rather, the relative decreases in intensity in both modes for the TCP–SLS material suggest the SLS [40] interacts with constituents within the C_3 and C_1 symmetry sites to effectively modulate (e.g. through possible Na^+ coordination to orthophosphate) or scatter (due to the anionic SO_4^- head group) IR signal at the orthophosphate positions. Ionic interactions between SLS and TCP likely occur since the C_3 site manifests both a void in the crystal lattice (i.e. the lack of an orthophosphate group) and an under-bonded

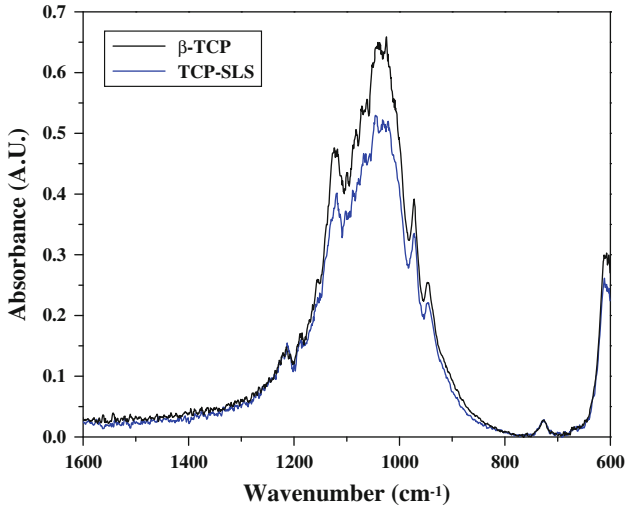

Fig. 3 IR vibrational spectra of β-TCP and TCP–SLS between 1,600 and 600 cm^{-1}

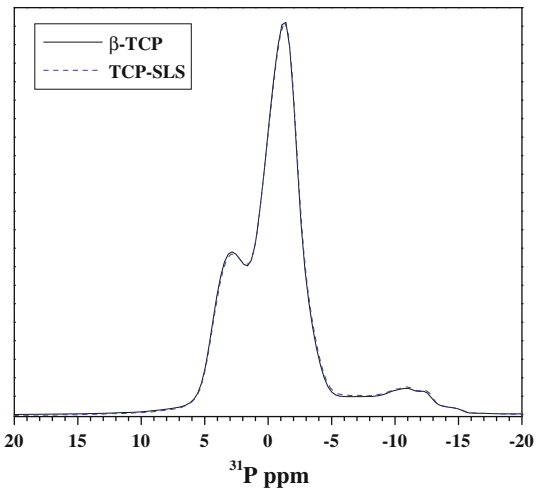

Fig. 4 Solid state ^{31}P NMR spectra of β-TCP and TCP–SLS

CaO_3 cluster. Qualitatively, Fig. 3 shows a strong relative decrease in peak intensities between 1,020 and 1,045 cm^{-1} in the TCP–SLS spectrum compared to β-TCP. Quantitatively, the β-TCP peak intensities at the 1,045 and 1,071 cm^{-1} positions are approximately 0.65 and 0.54 (resulting a peak-to-peak difference, Δ, of 0.11), while those same peak positions for TCP–SLS have intensities of 0.51 and 0.45 ($\Delta = 0.06$). Thus, the reduction in intensities in the v_3 bending region is clearly substantial and likely results from SLS coordination within the C_3 site. Modest intensity reduction is also observed for the C_1 sites (outside the 1,020–1,045 cm^{-1} range), so SLS apparently interacts with these environments, though less prominently and presumably through modification of the shared corner of the polyhedra connecting bound orthophosphate with CaO_n clusters as suggested previously [19]. In this case the coordination strength will vary for steric reasons with the bond length of CaO_8 slightly longer than that of CaO_7 [34]; as such, one can speculate that SLS primarily affects PO_4–CaO_8 coordination. Overall, these IR data clearly reveal changes in the fundamental v_1 and v_3 modes which in turn demonstrate the milling of SLS with β-TCP influences the TCP structural motif.

Solid-state ^{31}P NMR spectra comparing β-TCP and TCP–SLS are shown in Fig. 4. The relatively broad and less-intense features between -10 and -15 ppm can be associated with pyrophosphate [41] dimers and trimers, respectively, where orthophosphate structures are connected via one bridging oxygen. These features are consistent with the unique spectral features near 727 cm^{-1} in Fig. 3. The features centered about -1 and 3 ppm can be attributed to C_1 and C_3 orthophosphates, respectively, and are consistent with previous ^{31}P NMR results for tricalcium phosphate [42]. The ratio of the C_1:C_3 orthophosphate environments ($\sim$2.4) in Fig. 4 agrees very well with the expected orthophosphate ratio ($\sim$2.6) obtained through crystallographic analysis, where there are eight C_1 symmetry orthophosphate environments (two C_1 symmetry sites having four orthophosphate environments each) and three C_3 symmetry environments in the hexagonal unit cell structure.

The spectra in Fig. 4 clearly demonstrate short-range order is preserved in the β-TCP structure, despite the aggressive nature of the mechanochemical process. However, these results may not be surprising since the orthophosphate environments are not expected to undergo reactions with SLS to form dimers, trimers, or extended phosphate networks through the creation of bridging oxygens. Based on the IR spectra in Fig. 3, it is clear that SLS will primarily coordinate with underbonded CaO_3 entities, which in turn influences the nature of the bending modes of C_3 orthophosphate, and modestly contributes to PO_4–CaO_n modifications within the C_1 symmetry sites.

The solid-state ^{23}Na spectra in Fig. 5 indicate sodium imparts a role in the modification of β-TCP structure. While the majority of the sodium character observed in SLS and the TCP–SLS material are quite comparable, there are appreciable shoulders that develop near 15 and -3 ppm for the TCP–SLS material. These modest evolutions may be due to coordination of sodium to more shielded environments relative to the sulfate head group (SO_4^-); for instance, sodium may be coordinated to the orthophosphates residing in the TCP lattice, since these environments have at least two (in the C_1 symmetry site) and up to three (in the C_3 site) negative charges (e.g., PO_4^{2-} and PO_4^{3-}, respectively). Using exponential fitting functions, the T_1 relaxation of time for SLS (9.0 $\pm$ 0.3 ms) was measured to be significantly longer than that for TCP–SLS (8.0 $\pm$ 0.3 ms), which suggests that since sodium nuclei achieve

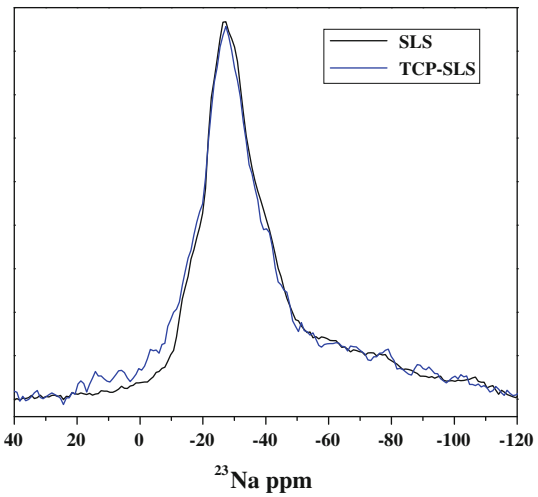

Fig. 5 Solid state ^{23}Na NMR spectra of β-TCP and TCP–SLS

equilibrium faster when interfaced with TCP, the coordination of sodium to entities within TCP may provide faster relaxation than sodium coordinated to the ionic sulfate head group of SLS. An independent ^{23}Na NMR experiment confirmed significantly low levels of sodium inherently in β-TCP and therefore the spectrum is not included in Fig. 5.

In addition to sodium coordination becoming affected due to interactions with β-TCP, the anionic surfactant portion is also affected as shown in Fig. 6. The 12-carbon chain of the SLS molecule can be mapped to the ^{13}C NMR spectra using Table 1, where carbon **1** is connected to the SO_4^- head group. These data are consistent with previously reported results [43]. The relative line narrowing for the TCP–SLS material suggests the interaction of SLS with TCP. Noticeably, the narrowing of the spectral feature of carbon **1** provides support that the ionic sulfate head group

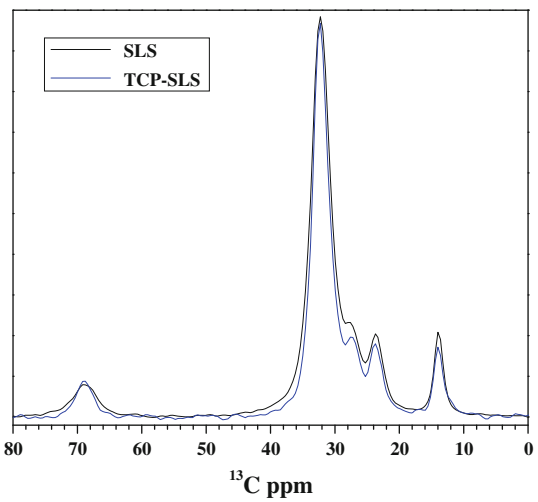

Fig. 6 Solid state ^{13}C NMR spectra of β-TCP and TCP–SLS

Table 1 ^{13}C chemical shifts along the sodium lauryl sulfate carbon chain

Carbon number in SLS	^{13}C ppm shift
1	68.8
2–9	32.3
10	27.6
11	23.7
12	14.0

is likely coordinated to CaO_n clusters (e.g., CaO_3 in the C_3 symmetry site) to effectively invoke some degree of order relative to native SLS. Further down the carbon chain the methyl environments **10** and **11** become more resolved in the presence of TCP and may be attributed to steric factors that may arise depending on where CaO_n coordination occurs in the TCP structure. To help quantify the difference in material properties between SLS and TCP–SLS, we performed T_1 measurements on the 32.3 ppm CH_2 spectral features. Using sigmoidal growth curves, the spin–lattice relaxation times were found to differ significantly, with SLS and TCP–SLS having constants of 0.82 ± 0.03 and 0.57 ± 0.03 s, respectively. The relatively shorter spin–lattice time for TCP–SLS likely indicates the sulfate head group coordinates with polyhedra, such as CaO_3, and this can be inferred qualitatively in looking at the spectral profile at the 68.8 ppm chemical shift. Further confirmation of this proposition might be confirmed with ^{43}Ca NMR experiments, however, investigation of calcium environments using NMR requires significant magnet strength and experimental time [44], and these stringent requirements are beyond the scope of our current studies. But based on our present data, we can further discuss probable TCP–SLS interactions with additional insight provided below.

We speculate that since CaO_7 and CaO_8 are relatively stable and encumbered polyhedra within the C_1 symmetry axes, SLS is more prone to coordinate to polyhedra within the C_3 site, where the combination of a missing orthophosphate polyhedron and the relatively small CaO_3 cluster provides significant opportunity for SLS coordination. Thus, to further explain the spectral features and contrasting T_1 times between β-TCP and TCP–SLS, it is important to assess the size of the vacancies within the C_3 symmetry site in relation to approximate SLS molecular size. The unit cell parameter along the c-axis for β-TCP is about 34.7 Å with about 22.2 Å of space occupied by calcium and phosphate polyhedra along at the C_1 symmetry site; conversely, only 10.4 Å is occupied at the C_3 symmetry site [34]. Hence, there is a crudely estimated vacancy of about 12 Å along the entire axis of the C_3 symmetry site. Due to the stabilized nature of the polyhedra packing (see Fig. 1 or [34]) the missing volume is likely to be

interrupted into physically-allowable fractions so a continuous 12 Å of vacancy is physically unrealistic. We can approximate the size of the SLS molecule (excluding the sulfate head group), R, to be approximately 5.2 Å if we consider the carbon backbone as a small polymer using the formula $R = N^{1/2}\ell$, where N, number of carbon atoms, is 12 and ℓ, the C–C bond length, is ~1.5 Å [45, 46]. If the bond lengths of S–O (~1.5 Å) and S–C (~1.8 Å) are also considered [46], the approximate size of the SLS molecule swells to 8.5 Å. Thus, this crude calculation shows that although vacancies within TCP may exist, these vacancies bear on the occupancy and positioning of the SLS molecule. Strain near the end of the SLS chain may well result due to repulsive interactions developing along the chain during entanglement, as well as through steric constraints that may arise from the rigidly fixed neighboring polyhedra lying within the C_3 symmetry site. These results are consistent with powder X-ray diffraction results (data not shown) that demonstrated minimal diffraction peak shifting (equivalent to or less than the employed 0.025° stepsize) relative to the β-TCP powder pattern. Such minimal shifting then strongly suggests the SLS molecule is unable to percolate throughout the β-TCP crystal structure but more likely coordinates ionically near the calcium polyhedra surfaces. Hence, these observations and speculations coincide with the NMR results.

Dissolution studies offer further insight into the nature of the TCP–SLS interactions. Solubility isotherms presented in Fig. 7 clearly show distinct trends for measured ionic calcium release over a period of 15 min, at which point steady-state conditions were reached. These trends clearly reveal differences among native β-TCP, milled β-TCP (mTCP, which was also milled for 2 h at 375 rpm), and TCP–SLS. To fit the data, an extended Langmuir model was used,

$$[Ca^{++}] = \frac{abt^{1-c}}{1 + bt^{1-c}} \quad (1)$$

with the lines through the data points indicating the theoretical modeling. $[Ca^{++}]$ corresponds to the measured ionic calcium activity obtained using the calcium-sensitive electrode; t represents dissolution time; a represents the concentration of calcium released from the TCP matrix after water contacts (or wets) the material and solvates calcium in a time b; c describes the ease of calcium release from the TCP matrix after contact and during solvation. The exponent, n, is defined as $1 - c$ and represents the overall power of time, and all fitting parameters are summarized in Table 2. Since the extended Langmuir model describes extended molecular coverage of one phase over another phase, we believe this model appropriately represents our system, where dissolution is described by the wetting and solvation of the solid matrix by water. In all cases, such curve fitting to the three data sets was shown to accurately model these physical processes.

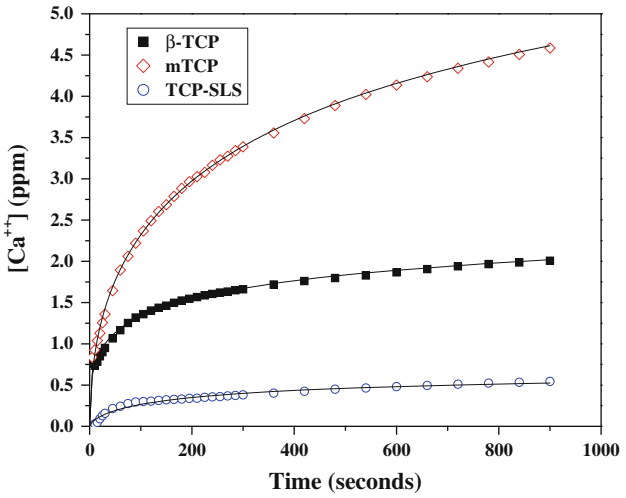

Fig. 7 Ca^{++} dissolution profiles for β-TCP, mTCP, and TCP–SLS. *Curves* were generated (as indicated by *solid lines*) by modeling the data to an extended Langmuir equation

Table 2 Fitting parameters associated with calcium availability for TCP materials modeled to an extended Langmuir equation

	β-TCP	mTCP	TCP–SLS
a	3.6 ± 0.4 ppm	8.8 ± 0.5 ppm	0.3 ± 0.1 ppm
b	0.12 ± 0.01 $s^{3/2}$	0.03 ± 0.01 s^2	0.03 ± 0.03 s^3
c	0.65 ± 0.03	0.49 ± 0.00	0.32 ± 0.08
R^2	0.992	0.998	0.972
χ^2	0.001	0.002	0.001
n	0.35	0.51	0.68

Noticeably, more than double the amount of ionic calcium, a, is released when β-TCP is milled relative to native β-TCP and this release occurs at a faster rate as described by the b, c, and n parameters. Presumably, the increased number of crystal faces that are affected during the grinding process of β-TCP accounts for the faster release and higher quantities of soluble calcium. However, the addition of SLS to β-TCP during the grinding process results in distinctly different solubility behavior. Apparently, the SLS molecule interacts with TCP to prevent ionic calcium activity (Ca^{++}) to be measured; nevertheless, calcium is still released as shown in the fitting parameters. The fitting parameter, b, clearly indicates water wets the TCP matrix very quickly and does so faster than for β-TCP and mTCP. Furthermore, the exponent parameter, n, indicates the dissolution rate is also higher than for β-TCP and mTCP. Apparently, the SLS molecule, through successful coordination to calcium polyhedra, essentially neutralizes

ionic calcium through the sulfate head group resulting in significant reduction in ionic calcium detectable with the calcium-sensitive electrode. Although anionic SLS interactions are expected to interact to some degree with different CaO_n polyhedra, we believe based on the structural experiments and assessments described in this paper, that these interactions are more likely to result at the underbonded CaO_3 site.

3.2 In vitro enamel remineralization using TCP–SLS and fluoride

The pH cycling model employed in this study accurately emulates clinical results for early caries reversal [4]. The alternating sequence of saliva-treatment-saliva-acid challenge-saliva-etc. is designed to mimic crystal seeding (i.e. treatment) and growth (i.e. saliva) events, as well as enamel weakening, or demineralization, events (i.e. acid challenge) that naturally occur during an eating event when cariogenic bacteria produce acids (i.e. lactic) during consumption of carbohydrates. Physiologically, the pH of the oral cavity drops to below 5.5 (the solubility of hydroxyapatite) leaving the enamel susceptible to 'white-spot', or subsurface lesion, formation, where the acids diffuse through the plaque fluid and pellicle layers to interface and dissolve apatite (i.e. demineralization) [47, 48]. These white-spots indicate the onset of caries and if not repaired (i.e. remineralized) ultimately progress to cavitations. The lesions are characterized by a mineral rich surface layer, which forms due to the pellicle and plaque fluid layers that inherently reside on the tooth surface to prevent 'free-flow' mineral loss from the tooth. Directly underneath the mineral-rich layer is the mineral-depleted layer, which extends to meet sound enamel with bowl-like concavity [49].

The present pH cycling study is employed to demonstrate the sensitivity to the remineralization of subsurface enamel lesions by fluoride. The groups used in this study include 5,000 ppm F (from NaF), which is typically dispensed by dental professionals in the US to high-risk caries patients needing stronger fluoride treatments relative to over-the-counter levels (i.e., between 900 and 1,150 ppm F) [2]. Figure 8 displays representative images of enamel cross-sections for the three treatment groups (DI water, 5,000 ppm F, and 5,000 ppm F plus TCP–SLS) after 5 days of cycling. The subsurface zones in the images are clearly shown relative to sound enamel, with significant decreases in the size of the subsurface zones observed for specimens treated with fluoride and fluoride plus TCP–SLS. These significant differences can be quantified with microhardness measurements. Figure 9 summarizes the net surface hardening (i.e. remineralization), measured using the Vickers indenter, of the enamel specimens after the pH cycling procedure. Vickers indentions are typically used in these experiments to assess the bulk response of hard-tissue, while the Knoops indentions discussed below are sensitive to thinner and/or smaller regions of material. Statistical analysis of the data clearly shows significant differences among the groups with Group 1 < Group 2 < Group 3. The clear statistical separation between the negative and positive control groups are consistent with dose–response [19, 35] and pilot results [50] and confirm utility of the remineralization/demineralization dental model selected for this study. Importantly, Group 3 with the TCP–SLS additive statistically outperformed the fluoride-only group (Group 2) with almost a 30% increase in enamel strength relative to fluoride alone. Further surface analysis shows the mean (±SEM) penetration depth of the Vickers indenter into the enamel surfaces for the three groups were as follows: 14.5 ± 0.3 μm (Group 1) > 9.1 ± 0.3 μm (Group 2) ≥ 8.5 ± 0.3 μm (Group 3). These results suggest either the nature or quantity of resultant mineral phases formed with fluoride plus TCP–SLS may be enhanced relative to fluoride alone. Based on these surface measurements, there appears to be a synergistic response to weakened dental tissue arising from the combination of 5,000 ppm F plus 800 ppm TCP–SLS.

To further characterize the extent of remineralization of subsurface enamel lesions, specimens were cross-sectioned and analyzed using the Knoops indenter. The trends in Knoops Hardness Number along the depth of the enamel cross-sections are expressed in Fig. 10. The sensitivity of the Knoops indenter enables one to judge the nature of the remineralized region at various depths within the subsurface lesion. The data shown in Fig. 10 clearly shows for all treatments, that sound enamel is achieved approximately 100 μm from the enamel surface. With respect to the DI water group, increased porosity and solubility of non-fluoridated apatite would result due to repeated exposures of demineralizing acid challenge events. Additionally, the extent of remineralization from exposure to fluoride-free artificial saliva would be limited due to the apparent poor mineral nucleation ability of calcium and phosphate of this mineral mix relative to fluoride (as shown in Figs. 9 and 10). Without effective nucleation, mineral growth is limited, which ultimately enables the acids during the acid challenge events to penetrate deeper into the enamel tissue, resulting in the leaching of apatite constituents (which includes calcium, phosphate, carbonate, etc.) from deep within the enamel tissue.

The longitudinal results on tissue treated with fluoride yield a distinctly different result compared to DI water treatment. The outer layers of enamel appear to be stabilized by fluoride, perhaps through the formation of fluoridated apatite, as measured at 12.5 μm from the enamel surface. Measurements made closer to the enamel surfaces were not feasible given the load limits and delicacy of the

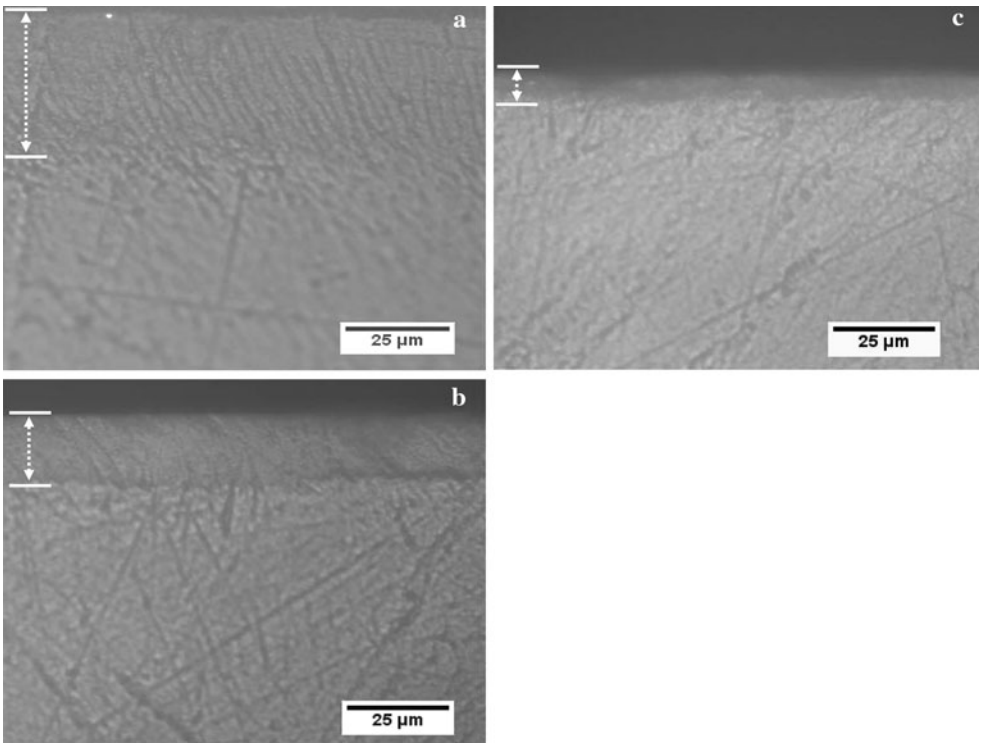

Fig. 8 Optical images showing the subsurface lesion and sound enamel cross-sections after 5 days of cycling when treated with **a** distilled (DI) water (negative control); **b** 5,000 ppm F (positive control); and, **c** 5,000 ppm F plus 800 ppm TCP–SLS. The bulk of the lesion area is indicated with the *white bars* and *arrow*

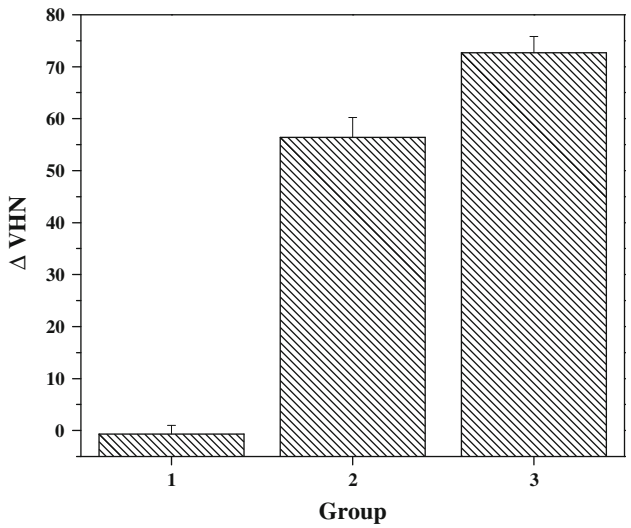

Fig. 9 Mean change in Vickers surface microhardness (*error bars* represent the standard error of the mean) of subsurface enamel lesions after 5 days of cycling for Group 1: distilled (DI) water (negative control); Group 2: 5,000 ppm F (positive control); and, Group 3: 5,000 ppm F plus 800 ppm TCP–SLS

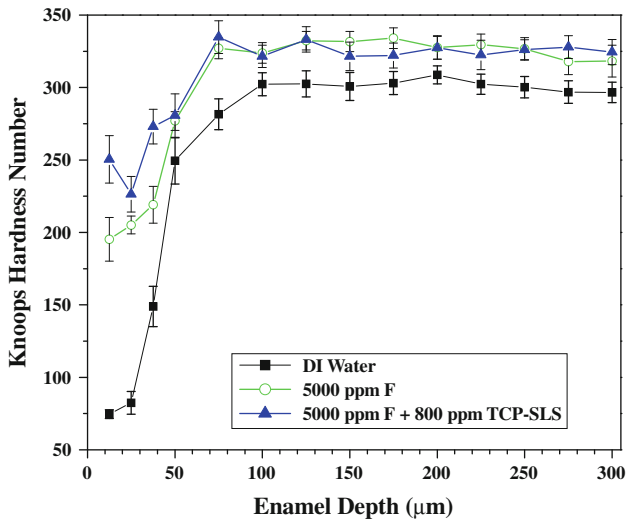

Fig. 10 Longitudinal change in mean Knoops microhardness (*error bars* represent the standard error of the mean) through the body of subsurface enamel lesions after 5 days of cycling. Enamel depth refers to distance from the outer enamel surface, which was exposed to the cycling regimen in the dental model and analyzed via Vickers microhardness measurements as shown in Fig. 9

specimens; nevertheless, the measurements made at 12.5 µm clearly demonstrate the strengthening effect of fluoride, with tissue treated with 5,000 ppm F plus 800 ppm TCP–SLS revealing a 30% stronger mineral phase relative to enamel treated with only fluoride and are consistent with results obtained in Fig. 8. These results suggest fluoride reacts with calcium phosphate phases in the tissue during remineralization periods (i.e. in artificial saliva) and/or

during treatment (i..e with TCP–SLS) to effectively promote seeding and crystal growth. Coupled with the high concentration and fast reaction kinetics of fluoride, which would greatly favor the formation of more acid-resistant fluoridated-mineral (such as fluorapatite), the tendency for significant demineralization to occur would be greatly reduced. In turn, porosity within the subsurface lesion would reduce, thus preventing extensive mineral leaching from the enamel interior. The steady repair of the subsurface lesion, however, may ultimately be modulated due to the nature of the 'newly-formed' surface layers; for instance, between 12.5 and 50 μm, the tissue response differs between Groups 2 and 3, with overall mineralization observed to be higher for tissue treated with fluoride plus TCP–SLS treatment. Apparently, the mineral formation processes for the TCP–SLS plus fluoride system results in a metastable condition whereby mineral seeding and growth may be competing between the surface and body of the lesion, and this may help explain the observed dip that occurs at 25 μm. This is further rationalized since the present dental model subjects the enamel specimens to constant cycling between remineralization and demineralization phases. In contrast, tissue treated with only fluoride appears to gradually repair the body of the lesion. Ultimately, at 50 μm the repair process appears to be comparable in both systems, thus suggesting the mineralization-limiting effect of 5,000 ppm F. These results and analysis are consistent with existing knowledge on the nature of caries formation and repair [51].

4 Conclusion

Employing a mechanochemical milling procedure, we constructed a functionalized form of β-TCP using sodium lauryl sulfate. The resultant material was then characterized using particle size analysis, IR spectroscopy, ^{31}P, ^{23}Na, and ^{13}C solid-state NMR experiments, and calcium solubility. Through analysis of the IR vibrational bands, spin–lattice relaxation times and short-range order, and dissolution kinetic profiles, the results strongly suggest SLS is coordinated to calcium oxide polyhedra, especially CaO_3, and influences orthophosphate character most notably along the C_3 symmetry axis manifested in the β-TCP lattice. The resultant hybrid material, which has been shown previously to be compatible with fluoride, was then evaluated with fluoride in an in vitro remineralization/demineralization dental model emulating the clinical situation. Using both surface and longitudinal microhardness analysis, we demonstrate statistically superior remineralization of subsurface enamel lesions for the combination of fluoride plus TCP–SLS relative to a clinically proven level of fluoride. These results demonstrate TCP–SLS can be combined with aqueous solutions of 5,000 ppm F to promote increased levels of enamel repair relative to fluoride alone and may bear on the formulation of future dental formulations aimed at reversing or slowing the progression of early carious lesions. Further studies are underway to reveal the mechanism of action for the TCP–SLS plus fluoride combination in remineralizing subsurface enamel lesions.

Acknowledgements This work was funded through an award from the Indiana 21st Century Research & Technology Fund. We kindly acknowledge Dr. John Edwards for technical assistance with NMR experiments.

References

1. Whelton H. Introduction: the anatomy and physiology of salivary glands. In: Edgar M, Dawes C, O'Mullane D, editors. Saliva and oral health. 3rd ed. London: British Dental Association; 2004. p. 1–13.
2. Tavss EA, Mellberg JR, Joziak M, Gambogi RJ, Fisher SW. Relationship between dentifrice fluoride concentration and clinical caries reduction. Am J Dent. 2003;16:369–74.
3. Featherstone JDB. Prevention and reversal of dental caries: role of low level fluoride. Community Dent Oral Epidemiol. 1999; 27:31–40.
4. White DJ. The comparative sensitivity of intra-oral, in vitro, and animal models in the 'profile' evaluation of topical fluorides. J Dent Res. 1992;71(Spec Iss):884.
5. Hodge HC, Smith FA. Fluorides and man. Annu Rev Pharmacol. 1968;8:395–408.
6. Hodge HC. Concentration of fluorides in drinking water to give the point of minimum caries with maximum safety. J Am Dent Assoc. 1950;40:436–9.
7. Schamschula RG, Barmes DE. Fluoride and health: dental caries, osteoporosis, and cardiovascular disease. Annu Rev Nutr. 1981;1: 427–35.
8. Marinho VCC, Higgins JPT, Logan S, Sheiham A. Topical fluoride (toothpastes, mouthrinses, gels or varnishes) for preventing dental caries in children and adolescents. Cocharane Database Syst Rev. 2003;4:Art. No. CD002782.
9. Selwitz RH, Ismail AI, Pitts NB. Dental caries. Lancet. 2007;369: 51–9.
10. Lussi A. Erosive tooth wear—a multifactorial condition of growing concern and increasing knowledge. In: Lussi A, editor. Dental erosion. Basel: Karger; 2006. p. 1–8.
11. Dye BA, Tan S, Smith V, Lewis BG, Barker LK, Thornton-Evans G, et al. Trends in oral health status: United States, 1988–1994 and 1999–2004. National Center for Health Statistics. Vital Health Stat. 2007;11(248).
12. Feagin F, Patel PR, Koulourides T, Pigman W. Study of the effect of calcium, phosphate, fluoride and hydrogen ion concentrations on the remineralization of partially demineralized human and bovine enamel surfaces. Arch Oral Biol. 1971;16:535–48.
13. Dedhiya MG, Young F, Higuchi WI. Mechanism of hydroxyapatite dissolution. The synergistic effects of solution fluoride, strontium, and phosphate. J Phys Chem. 1974;78:1273–9.
14. LeGeros RZ. Calcium phosphates in demineralization/remineralization processes. J Clin Dent. 1999;10:65–73.
15. Helena Y-U, Matti N, Timo N. Compound changes and tooth mineralization effects of glass ionomer cements containing

bioactive glass (S53P4), an in vivo study. Biomaterials. 2005;26: 5934–41.
16. Reynolds EC. Calcium phosphate-based remineralization systems: scientific evidence? Aust Dent J. 2008;53:268–73.
17. Kawska A, Brickmann J, Kniep R, Hochrein O, Zahn D. An atomistic simulation scheme for modeling crystal formation from solution. J Chem Phys. 2006;124:024513-024511–024513-024517.
18. Vogel GL, Shim D, Schumacher GE, Carey CM, Chow LC, Takagi S. Salivary fluoride from fluoride dentifrices or rinses after use of a calcium pre-rinse or calcium dentifrice. Caries Res. 2006;40:449–54.
19. Karlinsey RL, Mackey AC. Solid-state preparation and dental application of an organically-modified calcium phosphate. J Mater Sci. 2009;44:346–9.
20. Tung MS. Calcium phosphates: structures, composition, solubility and stability. In: Amiad Z, editor. Calcium phosphates in biological and industrial systems. Norwell: Springer; 1998. p. 1–20.
21. Zhang F, Chang J, Lu J, Lin K, Ning C. Bioinspired structure of bioceramics for bone regeneration in load-bearing sites. Acta Biomater. 2007;3:896–904.
22. Ghosh SK, Nandi SK, Kundu B, Datta S, De DK, Roy SK, et al. In vivo response of porous hydroxyapatite and beta-tricalcium phosphate prepared by aqueous solution combustion method and comparison with bioglass scaffolds. J Biomed Mater Res B. 2008;86:217–27.
23. Miao S, Cheng K, Weng W, Du P, Shen G, Han G, et al. Fabrication and evaluation of Zn containing fluoridated hydroxyapatite layer with Zn release ability. Acta Biomater. 2008;4:441–6.
24. Barkvoll P. Effect of sodium lauryl sulfate on the uptake of fluoride from NaF and MFP by etched enamel in vitro. J Biol Buccale. 1991;19:235–9.
25. Rodriguez-Hornedo N, Murphy D. Surfactant-facilitated crystallization of dihydrate carbamzepine during dissolution of anhydrous polymorph. J Pharm Sci. 2004;93:449–60.
26. White DJ. Reactivity of fluoride dentifrices with artificial caries I. Effects on early lesions: F uptake, surface hardening and remineralization. Caries Res. 1987;21:126–40.
27. ten Cate JM, Timmer K, Shariati M, Featherstone JDB. Effect of timing of fluoride treatment on enamel de- and remineralization in vitro: a pH-cycling study. Caries Res. 1988;22:20–6.
28. Schemehorn BR, Farnham RL, Wood GD, Stookey GK. A bovine enamel model for in vitro Remin/Demin tests. J Dent Res. 1990;69(Abstract #1213):260.
29. Featherstone JDB, Glena R, Shariati M, Shields CP. Dependence of in vitro demineralization of apatite and remineralization of dental enamel on fluoride concentration. J Dent Res. 1990;69(Spec Iss): 620–5.
30. ten Cate JM, Exterkate RAM, Buijs MJ. The relative efficacy of fluoride toothpastes assessed with pH cycling. Caries Res. 2006; 40:136–41.
31. Edmunds DH, Whittaker DK, Green RM. Suitability of human, bovine, equine, and ovine tooth enamel for studies of artificial bacterial carious lesions. Caries Res. 1988;22:327–36.
32. White DJ. Use of synthetic polymer gels for artificial carious lesion preparation. Caries Res. 1987;21:228–42.
33. Schemehorn BR, Stookey GK, Shuder BJ, Wood GD. Development of an in vitro incipient lesion remineralization/demineralization model. J Dent Res. 1986;65(Abstr 1177):300.
34. Yashima M, Sakai A, Kamiyama T, Hoshikawa A. Crystal structure analysis of β-tricalcium phosphate $Ca_3(PO_4)_2$ by neutron powder diffraction. J Solid State Chem. 2003;175:272–7.
35. Karlinsey RL, Mackey AC, Stookey GK, Pfarrer AM. In vitro assessments of experimental NaF dentifrices containing a prospective calcium phosphate technology. Am J Dent. 2009;22: 180–4.
36. Jillavenkatesa A, Condrate RA Sr. The infrared and Raman spectra of β- and α-tricalcium phosphate ($Ca_3(PO_4)_2$). Spectrosc Lett. 1998;31:1619–34.
37. Dayanand C, Bhikshamaiah G, Jaya TV, Salagram M, Krishna MA. Structural investigations of phosphate glasses: a detailed infrared study of the $x(PbO)$-$(1-x)P_2O_5$ vitreous system. J Mater Sci. 1996;31:1945–67.
38. Miztarzadeh F, Solati-Hashjin M, Salahi E. Study of conditions of synthesis of calcium phosphate bioceramics. Amirkabir. 1998;10:7–14.
39. Dantas AC, Greil P, Mueller FA. Effect of CO_2^{-3} incorporation on the mechanical properties of wet chemically synthesized β-tricalcium phosphate (TCP) ceramics. J Am Ceram Soc. 2008;91: 1030–3.
40. Lee K, Kunjappu J, Jockusch S, Turro NJ, Widerschpan T, Zhou J, et al. Amplification of the index of refraction of aqueous immersion fluids by ionic surfactants. Proc SPIE. 2005;5753: 537–53.
41. Kirkpatrick RJ, Brow RK. Nuclear magnetic resonance investigation of the structures of phosphate and phosphate-containing glasses: a review. Solid State Nucl Magn Reson. 1995;5:9–21.
42. Turner GL, Smith KA, Kirkpatrick RJ, Oldfield E. Structure and cation effects on phosphorous-31 NMR chemical shifts and chemical-shift anisotropies of orthophosphates. J Magn Reson. 1986;70:408–15.
43. Varshney M. Reassignment of ^{13}C NMR peaks of SDS micellar system by HMQC-NMR spectroscopy. Colloids Surf A. 1995;96:273–5.
44. Wong A, Howes AP, Dupree R, Smith ME. Natural abundance ^{43}Ca NMR study of calcium-containing organic solids: a model study for Ca-binding biomaterials. Chem Phys Lett. 2006;427: 201–5.
45. Grosberg AY, Khokhlov AR. Giant molecules. San Diego: Academic Press; 1997.
46. Pauling L. The nature of the chemical bond. 3rd ed. Ithaca: Cornell University Press; 1960.
47. Margolis HC, Moreno EC. Composition and cariogenic potential of dental plaque fluid. Crit Rev Oral Biol Med. 1994;5:1–25.
48. Edgar M, Higham SM. Saliva and the control of plaque pH. In: Edgar M, Dawes C, O'Mullane D, editors. Saliva and oral health. 3rd ed. London: British Dental Association; 2004. p. 86–102.
49. Applebaum E. The radiopaque surface layer of enamel and caries. J Dent Res. 1940;19:41–6.
50. Karlinsey RL, Mackey AC, Stookey GK. In vitro remineralization efficacy of NaF systems containing unique forms of calcium. Am J Dent. 2009;22:185–8.
51. Robinson C, Shore RC, Brookes SJ, Strafford S, Wood SR, Kirkham J. The chemistry of enamel caries. Crit Rev Oral Biol Med. 2000;11:481–95.